Ice sublimation in the dynamic HD 100453 disk reveals a rich reservoir of inherited complex organics

Booth, A.S.; Wölfer, L.; Temmink, M.; Calahan, J.; Evans, L.; Law, C.J.; ... ; Walsh, C.

Citation

Booth, A. S., Wölfer, L., Temmink, M., Calahan, J., Evans, L., Law, C. J., … Walsh, C. (2025). Ice sublimation in the dynamic HD 100453 disk reveals a rich reservoir of inherited complex organics. *Astrophysical Journal Letters*, *986*(1). doi:10.3847/2041-8213/adc7b2

The Astrophysical Journal Letters, 986:L9 (12pp), 2025 June 10 https://doi.org/10.3847/2041-8213/adc7b2

Ice Sublimation in the Dynamic HD 100453 Disk Reveals a Rich Reservoir of Inherited Complex Organics

Alice S. Booth[1,10], Lisa Wölfer[2], Milou Temmink[3], Jenny Calahan[1], Lucy Evans[4], Charles J. Law[5,11], Margot Leemker[6], Shota Notsu[7,8], Karin Öberg[1], and Catherine Walsh[9]

[1] Center for Astrophysics | Harvard & Smithsonian, 60 Garden St., Cambridge, MA 02138, USA; alice.booth@cfa.harvard.edu
[2] Department of Earth, Atmospheric, and Planetary Sciences, Massachusetts Institute of Technology, Cambridge, MA 02139, USA
[3] Leiden Observatory, Leiden University, 2300 RA Leiden, The Netherlands
[4] School of Physics and Astronomy, University of Leeds, LS2 9JT, UK; l.e.evans@leeds.ac.uk
[5] Department of Astronomy, University of Virginia, Charlottesville, VA 22904, USA
[6] Dipartimento di Fisica, Università degli Studi di Milano, Via Celoria 16, 20133 Milano, Italy
[7] Department of Earth and Planetary Science, Graduate School of Science, The University of Tokyo, 7-3-1 Hongo, Bunkyo-ku, Tokyo 113-0033, Japan
[8] Star and Planet Formation Laboratory, RIKEN Cluster for Pioneering Research, 2-1 Hirosawa, Wako, Saitama 351-0198, Japan
[9] School of Physics and Astronomy, University of Leeds, Leeds LS2 9JT, UK

Received 2025 March 7; revised 2025 March 25; accepted 2025 March 27; published 2025 June 5

Abstract

Protoplanetary disks around luminous young A-type stars are prime observational laboratories to determine the abundances of complex organic molecules (COMs) present during planet formation. In contrast to their lower stellar mass counterparts, these warmer disks contain the sublimation fronts of complex molecules such as CH_3OH on spatial scales accessible with the Atacama Large Millimeter/submillimeter Array (ALMA). We present ALMA observations of the Herbig Ae disk HD 100453 that uncover a rich reservoir of COMs sublimating from the dust cavity edge. In addition to CH_3OH, we detect $^{13}CH_3OH$ for the first time in a Class II disk, revealing a factor of three enhancement of ^{13}C in the disk large organics. A tentative detection of CH_2DOH is also reported, resulting in a D/H of 1%–2%, which is consistent with the expected deuterium enhancement from the low-temperature CH_3OH formation in molecular clouds and with the deuteration of CH_3OH measured in comets. The detection of methyl-formate (CH_3OCHO), at only a few percent level of CH_3OH, is an order of magnitude lower compared to claims toward other organic-rich Herbig Ae disks but is more in line with organic abundance patterns toward the earlier stages of star formation. Together these data provide multiple lines of evidence that disks, and therefore the planet- and comet-forming materials, contain inherited interstellar ices and perhaps the strongest evidence to date that much of the interstellar organic ice composition survives the early stages of planet formation.

Unified Astronomy Thesaurus concepts: Protoplanetary disks (1300); Astrochemistry (75); Complex organic molecules (2256); Radio astronomy (1338)

1. Introduction

Obtaining an inventory of the complex organic molecules (COMs; carbon- and hydrogen-based molecules containing six or more atoms) present across the different evolutionary stages of star and planet formation is fundamental when inferring the potential habitability of other worlds and the history of the organic matter in our solar system (E. Herbst & E. F. van Dishoeck 2009). With such inventories at hand we can trace the relative abundances of different molecules across these environments to look for both similarities and differences that can be linked to the physical and chemical conditions these molecules have experienced (J. K. Jørgensen et al. 2020). The focus of this work is to determine the complex organic composition of Class II disks, with the aim of further understanding how ices are inherited into planet-forming disks from the COM-rich pre- and protostellar stages of star formation (e.g., J. K. Jørgensen et al. 2016; S. Scibelli et al. 2021), and to infer whether this inherited material is transformed owing to heat and/or energetic processing during incorporation into the disk or throughout the disk lifetime (M. N. Drozdovskaya et al. 2014; C. Walsh et al. 2014).

The unique sensitivity of the Atacama Large Millimeter/submillimeter Array (ALMA) has enabled the first characterization of COMs in Class II disks (K. I. Öberg et al. 2015; C. Walsh et al. 2016; C. Favre et al. 2018). The initial detections of methyl-cyanide (CH_3CN) and methanol (CH_3OH) showed that these molecules are detectable but revealed new complications when trying to link these abundances to the potentially inherited disk ice reservoir. The abundant CH_3CN seen toward both T Tauri and Herbig Ae disks (J. B. Bergner et al. 2018; R. A. Loomis et al. 2018a; J. D. Ilee et al. 2021) has been shown to trace in situ UV-driven chemistry in the disk molecular layer, where the elemental carbon-to-oxygen ratio (C/O) is >1 (J. K. Calahan et al. 2023). Furthermore, the CH_3OH emission detected in the TW Hya disk traces the nonthermal desorption of CH_3OH ices from the outer disk, which is triggered by energetic particles, e.g., UV photons, and primarily results in the fragmentation of the CH_3OH molecule upon entering the gas phase (M. Bertin et al. 2016; C. Walsh et al. 2016, 2018). In both cases, the rotational temperatures of CH_3CN and CH_3OH are lower than expected from the thermal sublimation of COM-rich ices (J. D. Ilee et al. 2021; J. D. Ilee et al. 2025, in preparation); therefore, these observations are indirect tracers of the full COM reservoir.

---

[10] Clay Postdoctoral Fellow.
[11] NASA Hubble Fellowship Program Sagan Fellow.

In contrast, observations of transition disks around young Herbig Ae or F-type stars have revealed for the first time a thermally desorbed reservoir of COMs in Class II disks on scales of tens of au. CH_3OH has now been detected in three such systems and is found to be tracing warm (>100 K) gas most likely within the water snowline (A. S. Booth et al. 2021; N. van der Marel et al. 2021; A. S. Booth et al. 2023; M. Temmink et al. 2025; L. Evans et al. 2025). In this region of the disk, all of the COMs should be in the gas phase and are therefore all potentially observable to us with ALMA depending on their abundances. Indeed, dimethyl-ether (CH_3OCH_3), methyl-formate (CH_3OCHO), and ethelyne-oxide (c-C_2H_4O) have also been detected in a handful of these systems (N. G. C. Brunken et al. 2022; A. S. Booth et al. 2024a, 2024b; Y. Yamato et al. 2024a). Interestingly, the measured abundance ratios of these COMs relative to CH_3OH are inferred to be at least an order of magnitude higher than that measured toward younger protostars. These initial results indicate a potential increase in the complexity of the molecular ice reservoir during the disk lifetime, which could be explained via the conversion of CH_3OH ices into larger species as seen in laboratory experiments (e.g., L. J. Allamandola et al. 1988; P. A. Gerakines et al. 1996; K. I. Öberg et al. 2009). However, there are uncertainties in determining abundances from spatially and spectrally unresolved data, which may affect these results. If the underlying emitting area and/or the line optical depth of CH_3OH are underestimated, this may lead to overestimating the abundances of the other COMs (M. Temmink et al. 2025). One way to resolve this is via the detection of optically thinner CH_3OH transitions and CH_3OH isotopologues, which are now routinely obtained in line surveys of younger objects (e.g., V. Taquet et al. 2015).

This Letter presents ALMA observations of COMs in the disk associated with the binary system HD 100453. Located at 104 pc, the primary, HD 100453 A, is a 1.6 $M_\odot$ A9–F0 type star that hosts a dust- and gas-rich transition disk (J. Guzmán-Díaz et al. 2021; L. M. Stapper et al. 2024). The continuum emission from the disk around HD 100453 A (hereafter HD 100453), as viewed by ALMA, is composed of an outer dust disk with a radius from ≈16 to 53 au, a position angle of 145°, and an inclination of 35° and a small inner disk <1 au (G. P. Rosotti et al. 2020). VLTI/GRAVITY observations show that this inner disk is significantly misaligned with respect to the outer disk, resulting in prominent shadows in the outer disk when viewed in scattered light (M. Benisty et al. 2017; A. J. Bohn et al. 2022). Beyond the outer disk of HD 100453, at ≈120 au, is the orbital location of the young M4 star HD 100453 B (K. Wagner et al. 2015). The dynamical interactions between the companion star and the disk drive two spiral arms traced in both scattered light and CO gas kinematics (K. A. Collins et al. 2009; K. Wagner et al. 2015, 2018; G. P. Rosotti et al. 2020). The molecular makeup of the HD 100453 disk was surveyed by G. V. Smirnov-Pinchukov et al. (2022), where $C^{18}O$, HCO^+, HCN, CN, and CS are all detected in ≈1″-resolution ALMA data. Notably, they report a nondetection of C_2H, hinting at a low C/O in the gas phase. In this work we report the detections of new molecular species in the HD 100453 disk, including $^{13}CH_3OH$ for the first time in a Class II disk. In Section 2 we describe the observations, in Section 3 we share the results, and in Sections 4 and 5 we discuss these results and summarize our conclusions.

2. Methods

HD 100453 was observed with ALMA in Band 7 in two spectral setups within project 2023.1.00252.S (P.I. A. Booth). The first spectral setting was executed on 2024 May 13 and 14 for a total time of 2.6 hr, with baselines ranging from 15 to 783 m and 46 antennas on both occasions. The second setting was executed on 2024 May 13, September 4, and September 29 with the same overall baseline range as the former setting, for a total time of 3.7 hr, and with 47, 36, and 43 antennas, respectively, for each execution. The smallest maximal recoverable scale probed by these data is 4″.0, which is significantly larger than the ≈2″.0 diameter of the ^{12}CO gas disk (e.g., G. van der Plas et al. 2019). The two spectral setups are in the 290–315 GHz range, and each consists of 12 spectral windows, all of which have a channel width of 488.281 kHz (0.51 km s^{-1} at 290 GHz).

The data for each setting were calibrated and self-calibrated within the ALMA data reduction pipeline by ALMA staff using CASA version 6.5.5 (J. P. McMullin et al. 2007). Each of the measurement sets was continuum subtracted in CASA using a fit order of 1, and all channels with clear line detections were excluded from the fit. An initial line identification was performed using matched filtering with Keplerian models (R. A. Loomis et al. 2018b). These models were Boolean masks tracing the expected Keplerian rotation of the disk gas based on the aforementioned position and inclination angles of the CO gas disk as traced by ALMA with a range of radial extents. The data were then imaged with `tCLEAN` using a Briggs robust parameter of 2.0 to maximize line detection sensitivity and a conservative analytical Keplerian mask. Images were generated with a channel width of 0.55 km s^{-1} with rms noise levels ranging from 1.0 to 1.6 mJy $beam^{-1}$. The resulting average beam size for the images is 0″.55 × 0″.48 (60°) for setting 1 and 0″.67 × 0″.63 (−69°) for setting 2.

The integrated intensity maps were generated from the image cubes using a 1″.0 Keplerian mask[12] and the Python package `BetterMoments`.[13] Spectra were extracted both from a 0″.5-radius circular mask centered at the position of HD 100453 A and from a Keplerian mask with the same radial extent. This mask size is ≈2× the beam size and was found to be sufficient to encapsulate all of line flux while minimizing the inclusion of noisy pixels. The disk-integrated flux was then calculated from the masked spectra, and for nondetections a 3σ upper limit on the flux was determined where σ is propagated from the rms in the line-free channels and the number of pixels included in the mask (e.g., M. T. Carney et al. 2019). These fluxes are used in a now-standard rotational diagram analysis to determine the column density and rotational temperature of the gas, including an optical depth correction (e.g., R. A. Loomis et al. 2018a; J. Pegues et al. 2020; M. Temmink et al. 2023). In the case in which the lines are detected in both of the spectral settings we include an additional 10% error to account for the absolute flux calibration uncertainty of ALMA. In the rotational diagram analysis, we used the Markov Chain Monte Carlo implementation of the emcee-package (D. Foreman-Mackey et al. 2013) to obtain posterior distributions of the column density and rotational temperature. Where we do not have enough transitions for a rotational diagram approach, we fix the temperature. The details on the emitting area and line width used for these calculations are discussed in Section 3.

---

[12] https://github.com/richteague/keplerian_mask

[13] https://github.com/richteague/bettermoments

Table 1
Molecular Data and Disk-integrated Fluxes and Upper Limits of the Transitions Analyzed in This Work

Molecule	Transition	Frequency (GHz)	$\log(A_{\rm ul})$ (s^{-1})	$E_{\rm up}$ (K)	$g_{\rm ul}$	Beam (″ × ″ (deg))	Integrated Flux ± Error (mJy km s^{-1})
$^{13}C^{18}O$	3–2	314.119653	−5.723	30.2	7	0.67 × 0.63 (-69.0)	20.2 ± 5.6
HDO	6(2,5)–5(3,2)	313.750620	−4.426	553.7	13	0.66 × 0.63 (−67.0)	<16.8
H_2CO	4(1,3)–3(1,2)	300.836636	−3.144	47.8	27	0.38 × 0.32 (−51.0)	340.7 ± 17.1
H_2CO	4(2,2)–3(2,1)	291.948067	−3.280	82.1	9	0.54 × 0.46 (65.0)	122.0 ± 6.4
H_2CO	4(3,2)–3(3,1)	291.380442	−3.517	140.9	27	0.57 × 0.49 (58.0)	165.7 ± 7.0[a]
H_2CO	4(3,1)–3(3,0)	291.384362	−3.517	140.9	27	0.57 × 0.49 (58.0)	165.7 ± 7.0[a]
$H_2^{13}CO$	4(1,3)–3(1,2)	293.126515	−3.178	47.0	27	0.51 × 0.46 (66.0)	16.1 ± 5.5
CH_3OH	1(1,0)–1(0,1)	303.366921	−3.493	16.9	12	0.55 × 0.47 (57.0)	129.1 ± 8.5
CH_3OH	2(1,1)–2(0,2)	304.208348	−3.490	21.6	20	0.52 × 0.45 (64.0)	148.7 ± 8.9
CH_3OH	3(1,2)–3(0,3)	305.473491	−3.486	28.6	28	0.49 × 0.44 (68.0)	147.3 ± 8.8
CH_3OH	6(1,5)–5(1,4)	292.672889	−3.975	63.7	52	0.67 × 0.63 (−64.0)	143.0 ± 8.4
CH_3OH	6(1,5)–6(0,6)	311.852612	−3.466	63.7	52	0.57 × 0.48 (58.0)	140.6 ± 8.4
CH_3OH	7(1,6)–7(0,7)	314.859528	−3.456	80.1	60	0.66 × 0.62 (−69.0)	140.2 ± 7.2
CH_3OH	7(−1,6)–6(−2,5)	313.596760	−4.327	86.0	60	0.66 × 0.63 (−67.0)	76.2 ± 7.8
CH_3OH	12(0,12)–11(1,11)	302.912979	−3.815	180.9	100	0.68 × 0.64 (−63.0)	107.6 ± 5.8
CH_3OH	10(-5,5)–11(-4,7)	302.830740	−4.569	263.7	84	0.68 × 0.64 (−63.0)	46.6 ± 4.8
CH_3OH	4(1,4)–5(2,4)	312.247362	−3.825	348.4	36	0.67 × 0.63 (−63.0)	37.9 ± 4.6
CH_3OH	18(1,18)–17(2,15)	306.291135	−4.283	407.6	148	0.49 × 0.44 (68.0)	47.3 ± 6.1
CH_3OH	17(6,11)–18(5,14)	291.908215	−4.482	548.6	140	0.57 × 0.48 (58.0)	14.8 ± 7.3
CH_3OH	12(-8,5)–12(-7,5)	294.256085	−4.009	775.7	100	0.51 × 0.46 (67.0)	19.2 ± 7.2
$^{13}CH_3OH$	3(1,2)–3(0,3)	305.699456	−3.485	28.3	7	0.49 × 0.44 (70.0)	30.1 ± 6.6
$^{13}CH_3OH$	6(1,5)–6(0,6)	311.773919	−3.466	62.5	13	0.67 × 0.63 (−64.0)	31.9 ± 5.4
$^{13}CH_3OH$	7(1,6)–7(0,7)	314.635901	−3.457	78.5	15	0.66 × 0.62 (−69.0)	35.4 ± 5.6
$^{13}CH_3OH$	10(0,10)–9(1,8)	302.590285	−4.160	137.5	21	0.68 × 0.64 (−63.0)	11.6 ± 4.3
CH_2DOH	7(2,6)–6(2,5) o1	312.324908	−3.915	95.5	15	0.66 × 0.63 (−67.0)	21.2 ± 4.9[a]
CH_2DOH	7(2,6)–6(2,5) e1	312.322940	−3.932	86.5	15	0.66 × 0.63 (−67.0)	21.2 ± 4.9[a]
CH_3CN	17(0)–16(0)	312.687743	−2.737	135.1	70	0.66 × 0.63 (−67.0)	42.9 ± 5.7
CH_3CN	17(1)–16(1)	312.681731	−2.739	142.2	70	0.66 × 0.63 (−67.0)	35.1 ± 5.4
CH_3CN	17(2)–16(2)	312.663700	−2.743	163.6	70	0.66 × 0.63 (−67.0)	27.2 ± 6.0
CH_3CN	17(3)–16(3)	312.633653	−2.751	199.4	140	0.66 × 0.63 (−67.0)	21.0 ± 5.4
CH_3OCHO	27(1,27)–26(1,26) A	291.111871	−3.428	198.6	110	0.52 × 0.46 (68.0)	38.4 ± 5.1[a]
CH_3OCHO	27(0,27)–26(0,26) A	291.111891	−3.428	198.6	110	0.52 × 0.46 (68.0)	38.4 ± 5.1[a]
CH_3OCHO	27(1,27)–26(1,26) E	291.111192	−3.428	198.6	110	0.52 × 0.46 (68.0)	38.4 ± 5.1[a]
CH_3OCHO	27(0,27)–26(0,26) E	291.111212	−3.428	198.6	110	0.52 × 0.46 (68.0)	38.4 ± 5.1[a]
CH_3OCH_3	16(1,16)–15(0,15) EA	292.412244	−3.705	120.3	198	0.51 × 0.46 (66.0	<22.0[a]
CH_3OCH_3	16(1,16)–15(0,15) EA	292.412244	−3.706	120.3	132	0.51 × 0.46 (66.0	<22.0[a]
CH_3OCH_3	16(1,16)–15(0,15) EE	292.412416	−3.705	120.3	528	0.51 × 0.46 (66.0	<22.0[a]
CH_3OCH_3	16(1,16)–15(0,15) AA	292.412588	−3.705	120.3	330	0.51 × 0.46 (66.0	<22.0[a]

Note. All molecular data are taken from the Cologne Database for Molecular Spectroscopy (H. S. P. Müller et al. 2001, 2005) where available for consistency. The data for CH_3OCHO, HDO, and CH_2DOH are from the Molecular Spectroscopy and Line Catalogs collated by the NASA Jet Propulsion Laboratory (H. M. Pickett et al. 1998).

[a] Blended transition of the same molecule where the flux reported is the sum of both components.

3. Results

3.1. Emission Morphology and Kinematics

In total we detect five organic molecules in the HD 100453 disk above the 5σ level in the disk-integrated fluxes that are extracted from Keplerian masks. These molecules are H_2CO, CH_3OH, $^{13}CH_3OH$, CH_3CN, and CH_3OCHO. In addition, we also detect the rare CO isotopologue $^{13}C^{18}O$. We also identify CH_2DOH at the 4σ level in the disk-integrated line flux and $H_2^{13}CO$ at the 3σ level. The list of different transitions detected for each molecule is shown in Table 1, along with the associated disk-integrated line fluxes and errors. Within these data we note the detection of the H_2CO $J = 4(2,3)-3(2,2)$ and CH_3OH $J = 15(1,14)$–$14(2,13)$ transitions, but these are blended in velocity space and are therefore excluded from the analysis. In addition, the CH_3OH $J = 17(6,11)$–$18(5,14)$ line is only detected at a 2σ significance level, but as it follows the same line shape as the other transitions, we include this data point and the associated error in our subsequent analysis. In Table 1, we also list a select number of transitions that went undetected for molecules of particular interest, HDO and CH_3OCH_3, and their associated upper limits.

Figure 1 presents the Keplerian-masked integrated intensity maps of a subset of the detected lines in the HD 100453 disk

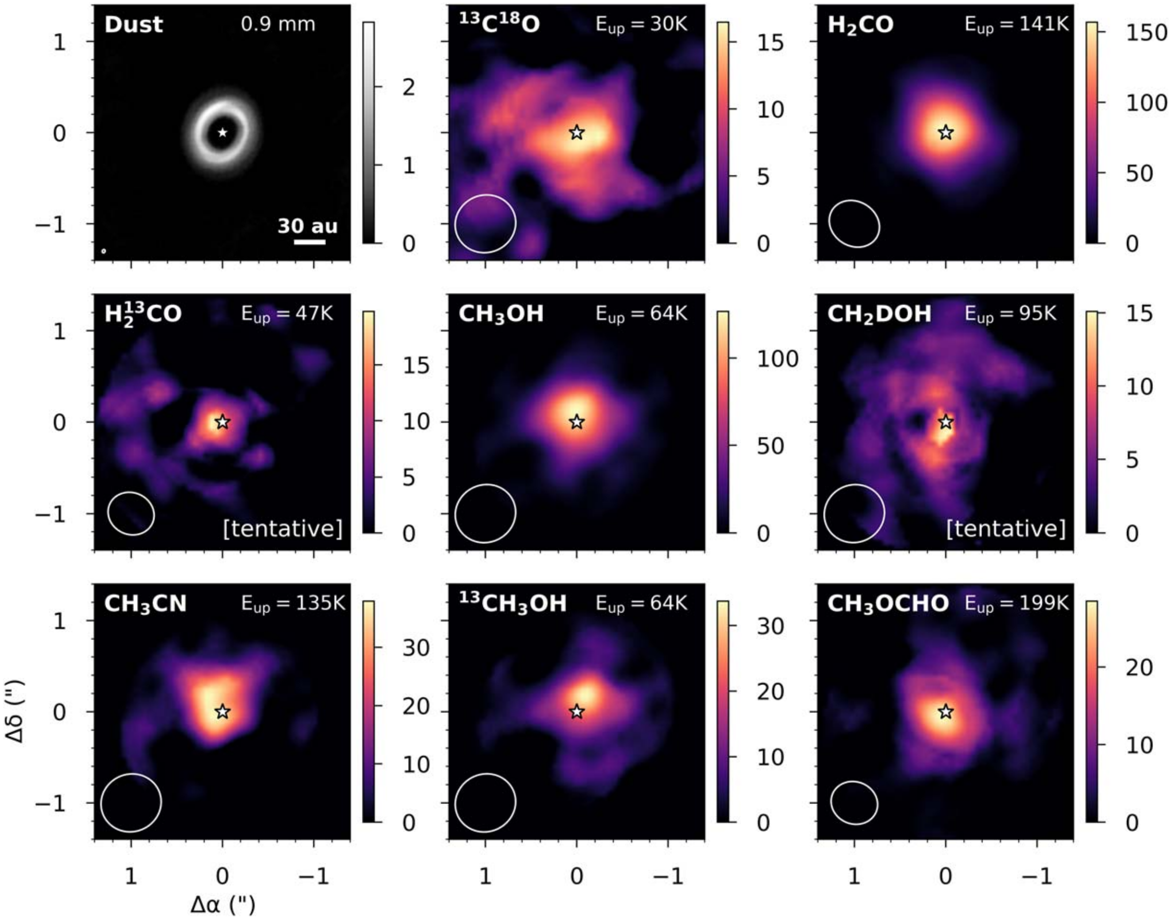

Figure 1. Integrated intensity maps of the 0.9 mm dust continuum emission (taken from G. P. Rosotti et al. 2020) and molecular line emission from the HD 100453 disk. For the line maps, the text in the upper right corner notes the upper energy level of the transition shown (see Table 1), and in all plots the beam is shown in the lower left corner of each panel. The units of the color bar are mJy beam^{-1} km s^{-1} for the molecular lines and mJy beam^{-1} for the continuum, and the position of HD 100453 A is marked with a star.

alongside the higher angular resolution 0.9 mm continuum observations from G. P. Rosotti et al. (2020). All of the molecular emission is compact with respect to the beam and appears to be cospatial. Of note are the $J = 6(1,5)–6(0,6)$ ($E_{\rm up} = 64$ K) transitions of CH_3OH and $^{13}CH_3OH$, which show only a factor ≈3.3 difference in peak values in their respective integrated intensity maps. This low value when compared to the $^{12}C/^{13}C$ ratio of ≈69 expected for the local interstellar medium (ISM) likely indicates optically thick emission from the main CH_3OH isotopologue for this transition (T. L. Wilson 1999).

The extracted spectra of the 13 total isolated CH_3OH lines that cover a range in upper energy levels from 17 to 776 K are shown in Figure 2. In addition to CH_3OH, we also detect four lines of $^{13}CH_3OH$, and these spectra are shown in Figure 3 alongside the spectra for CH_3CN, CH_3OCHO, and the other tentative and nondetections of note. Given the large cavity in millimeter-dust emission, we would expect ringed emission from these species although we do not have the spatial resolution to resolve this in the image plane. To increase the relative signal-to-noise ratio in the CH_3OH spectra, we also show the average spectra calculated from the first eight transitions listed in Table 2. This was generated by regridding and stacking eight individual measurement sets that were split out around each of the lines. These steps were performed using the CASA tasks `mstransform` and `concat`. These measurement sets were then concatenated and imaged, and the spectra were extracted following the same procedure as for the individual line images. The CH_3OH line wings drop off sharply at approximately −5.5 and +5.0 km s^{-1} relative to the source velocity of 5.25 km s^{-1}. The difference in the red and blue wings of the line may indicate an underlying asymmetry in the gas emission, but it is within one velocity channel of the data. If we assume an inclination angle of 35° and a stellar mass of 1.6 $M_\odot$, the average velocity of the line wings is consistent with a radial distance of ≈17 au. Therefore, these line wings are tracing gas at the millimeter-dust cavity edge.

The lines also show an interesting morphology with three emission peaks compared to the expected double-peaked profile associated with the Keplerian rotation of a ring of gas. To place this in context with the bulk gas of the disk, we also show in Figure 2 the total disk-integrated spectra of the ^{12}CO $J = 3–2$ line; these data are presented fully in G. P. Rosotti et al. (2020) and L. Wölfer et al. (2023). Compared to the CH_3OH, the CO line wings trace higher velocities, therefore tracing gas closer to the star, within the dust cavity, but interestingly there is a similar bump in the spectra around the source velocity as seen in the CH_3OH. To investigate the morphology of the CH_3OH emission further, we imaged the stacked data at lower robust values of +0.5, −0.5, and −2.0. The resulting integrated intensity maps, peak emission maps, and peak velocity maps are shown in Figure 4, and the

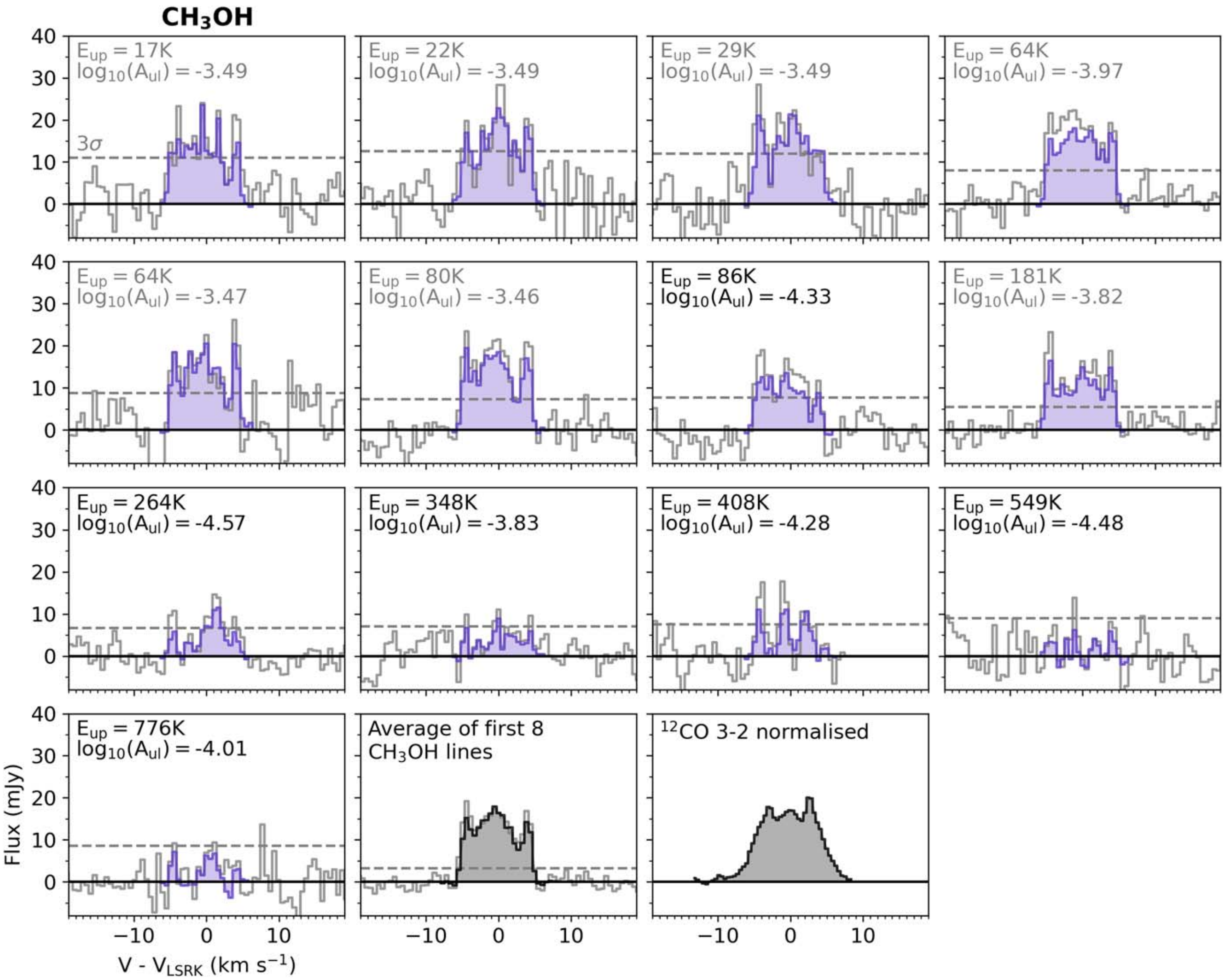

Figure 2. CH_3OH emission-line spectra extracted from a 0″.5-radius circular aperture centered on source (gray) and from a Keplerian mask with the same radial extent (purple/black). The black and gray font colors for the upper energy levels and Einstein coefficients match those in Figure 5, where only the black points are used in the rotation diagram analysis. The dashed line marks the 3σ level for the spectra from the circular aperture. This is an overestimate of the errors in the masked spectra but provides a good gauge of the significance of the detections. The final panel shows normalized ^{12}CO $J = 3$–2 disk-integrated spectra for comparison, where the data are first presented in G. P. Rosotti et al. (2020).

properties of the images are listed in Table 2. When going to higher resolution, the emission becomes more compact and there is a clear offset in the integrated intensity to the northeast of the disk. This excess on the minor axis may reflect the excess emission at the source velocity highlighted in the spectra.

3.2. Rotational Temperatures and Column Densities

Due to the number of lines of CH_3OH, $^{13}CH_3OH$, and CH_3CN detected and the range in upper energy levels these transitions span, we are able to calculate empirical rotational temperatures and column densities for each of these species (as listed in Table 3). We iterate these calculations such that the thermal line width used to determine the optical depth is consistent with the recovered rotational temperature. The equations for the optical depth and thermal line width are fully described in R. A. Loomis et al. (2018a) and J. Pegues et al. (2020). Within this framework we require an underlying emitting area of the gas, which we assume is the same for all of the organic molecules. Given the sharp drop-off in the CH_3OH line wings, we set the inner radius of this area to be the inner edge of the millimeter dust and the outer radius to be half of the major axis for the beam for the briggsrobust = −2.0 stacked CH_3OH image (as shown in Figure 4). This results in a ring of gas from 16 to 30 au (note that the size of the $C^{18}O$ gas disk is ≈60 au; L. M. Stapper et al. 2024). Although there are hints at nonaxisymmetric emission structures in these higher-resolution images, we do not have the sensitivity to determine this on a line-by-line basis, and therefore we adopt a simple disk-averaged column density approach. Our absolute column densities will therefore scale inversely with the chosen emitting area, as is typical, but we are most interested in the abundance ratios between different species and the rotational temperatures, which are not effected by this assumption when in the optically thin regime.

In Figure 5 we show the resulting rotational diagrams for CH_3OH, $^{13}CH_3OH$, and CH_3CN. For CH_3OH there is a clear scatter in the diagram, likely due to a range of line opacities probed by our data. To mitigate this, we only include lines with Einstein A-coefficients lower than 10^{-4} s^{-1} and/or upper energy

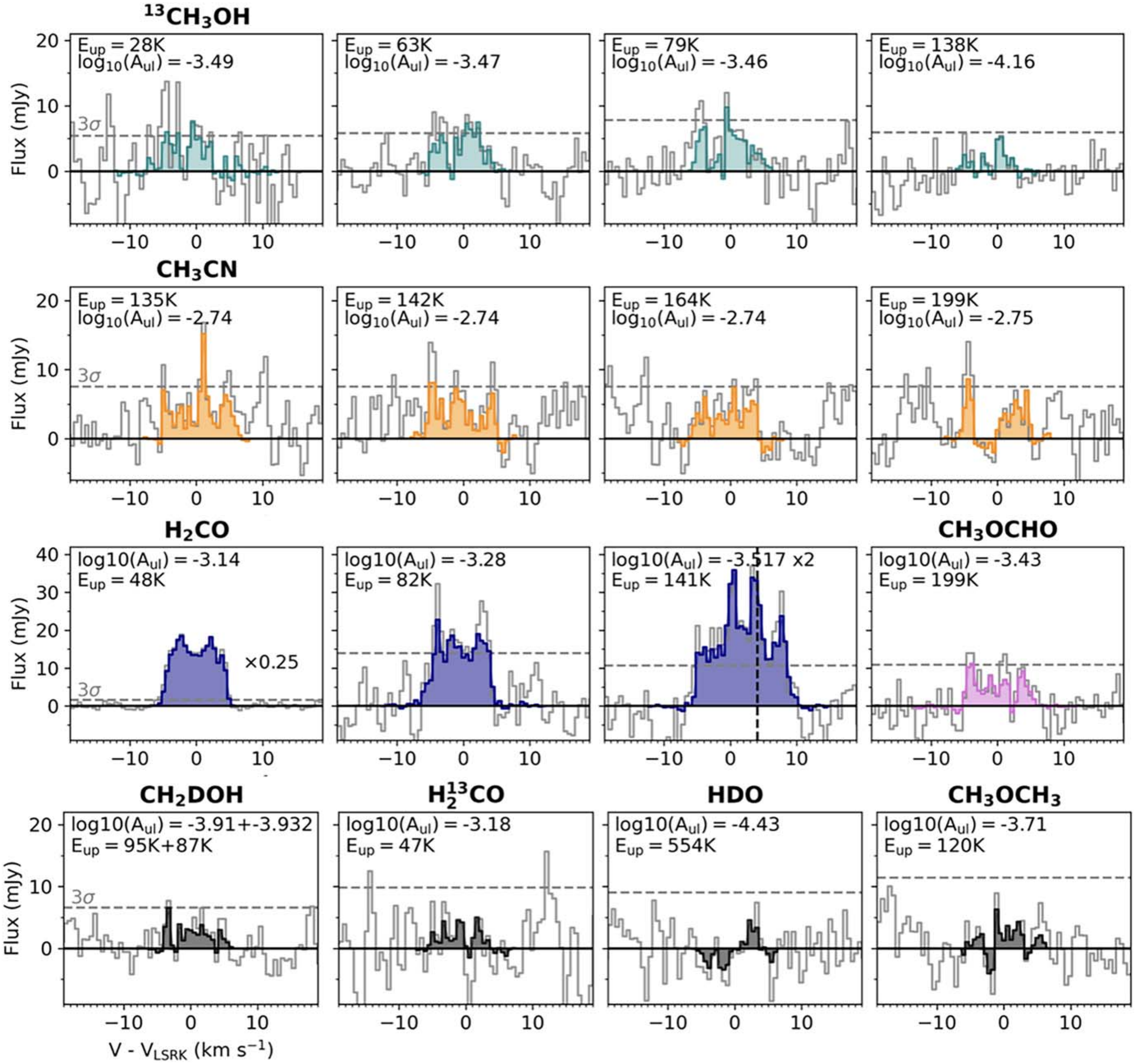

Figure 3. Same as Figure 2, but for the other molecular lines in the data.

Table 2
Properties of the Stacked CH_3OH Images

Robust	Beam ($'' \times ''$ (deg))	rms[a] (mJy beam^{-1})	Peak Intensity (mJy beam^{-1})
+2.0	0.60 × 0.55 (87)	0.50	13.44
+0.5	0.43 × 0.39 (−90)	0.55	12.18
−0.5	0.30 × 0.28 (70)	1.02	10.55
−2.0	0.28 × 0.27 (56)	1.41	11.84

Note.
[a] Per 0.55 km s^{-1} channel.

levels greater than 300 K in the linear fit. These are highlighted in Figure 5 via the color of the scatter points, where only the black, and not the grey points, are included in the fit. All of the lines in this subset have optical depths <0.09, and the CH_3OH column density is well constrained to ≈1.6 × 10^{16} cm^{-2} with a rotational temperature of ≈230 K. The $^{13}CH_3OH$ fit retrieves a column density of ≈7.5 × 10^{14} cm^{-2} and a somewhat lower temperature, but when considering the uncertainties, it is consistent with that for CH_3OH. We discuss the $^{12}C/^{13}C$ ratio further in Section 4.3 The results for CH_3CN are notably different, with a cooler rotational temperature of ≈50 K and a much lower column density of ≈4.0 × 10^{13} cm^{-2}. We attempted the same analysis for H_2CO, but the 4(1,3)–3(1,2) and 4(2,2)–3(2,1) transitions were found to be optically thick with $\tau \geqslant 1$. For the column density estimates of H_2CO, CH_3OCHO, CH_2DOH, and $H_2^{13}CO$, as well as the upper limits on HDO and CH_3OCH_3, we calculate these at the fixed temperature of 228 K determined from the CH_3OH, as we expect these species to sublimate at approximately the same region of the disk. These results are listed in Table 3 alongside the relative percentage abundances of these species with respect to CH_3OH. We find that all of the species are present at less than the 5% level.

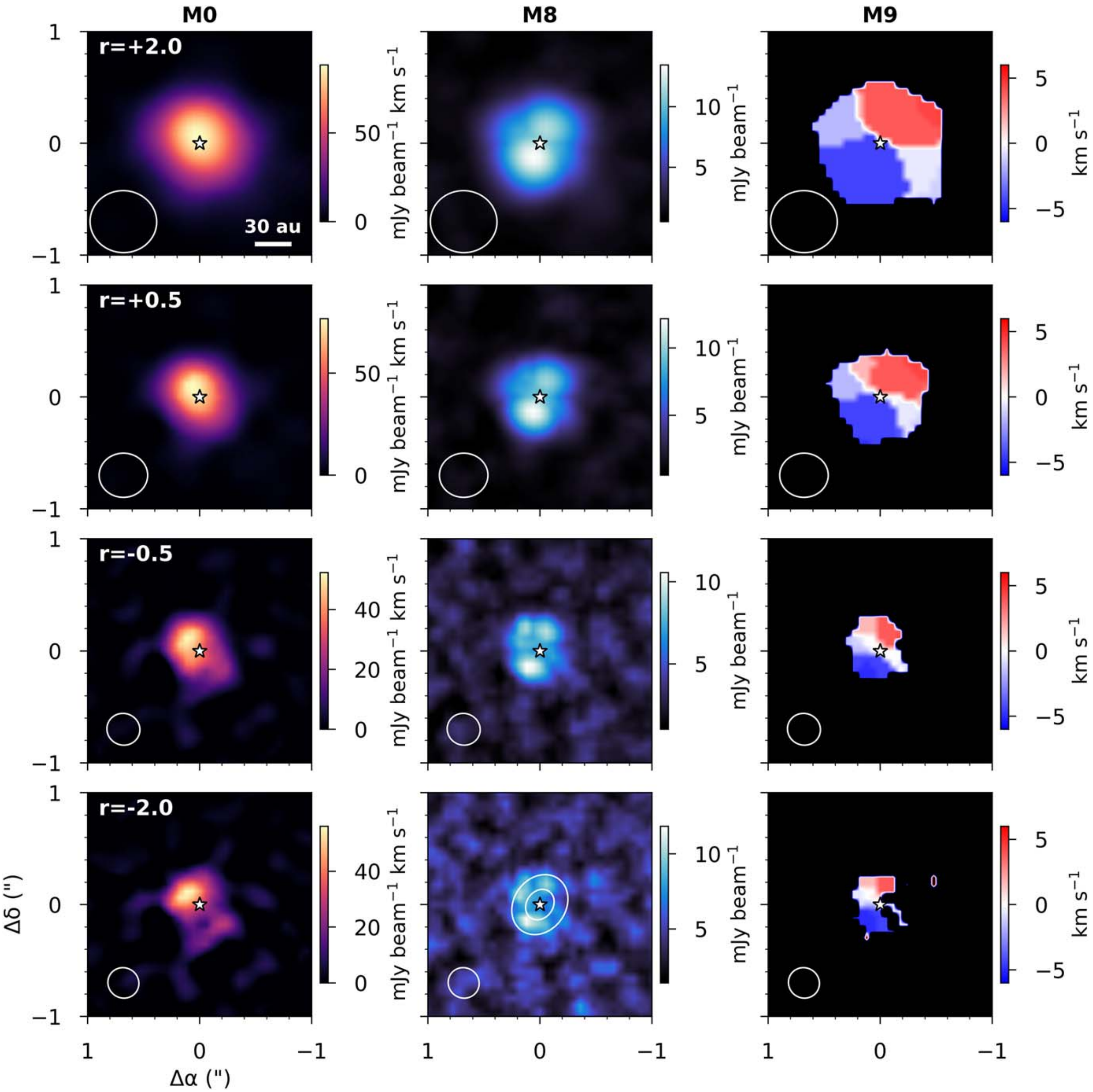

Figure 4. Moment maps of the stacked CH_3OH lines imaged at different robust parameters [+2.0, +0.5, −0.5, −2.0]. From left to right the maps are the Keplerian-masked integrated intensity (M0), peak intensity (M8), and peak velocity (M9) maps. In the center map the color bar starts at the 3σ level, and the right maps have had a 5σ clip applied to the channel maps. The ellipses in the middle panel of the bottom row highlight the ringed area used to calculate the column densities.

4. Discussion

4.1. The Physical Origin of COMs in the HD 100453 Disk

Our results show that the HD 100453 disk has a rich reservoir of COMs. The CH_3OH line wings and rotational temperature corroborate that we are likely tracing a ring of gas originating from the thermal sublimation of CH_3OH-rich ices at the inner dust cavity edge, very similar to the scenario first proposed for the HD 100546 disk (A. S. Booth et al. 2021). Looking at complementary tracers of the disk gas temperature, the optically thick ^{12}CO lines do reach brightness temperatures of ≈100 K in the vicinity of the dust cavity (L. Wölfer et al. 2023). Given these lines of evidence, we infer that the CH_3OH isotopologues and CH_3OCHO detected in the HD 100453 system also originate from thermally sublimating ices close to the dust cavity wall. The lower rotational temperature of CH_3CN relative to CH_3OH may indicate a different physical origin for this species, which will be discussed further in Section 4.2.

Notably, L. Wölfer et al. (2023) show a temperature asymmetry in the HD 100453 disk, where the CO gas in the northeast of the disk is warmer. Interestingly, this is the same region of the disk where we see the excess CH_3OH when imaging the data at higher angular resolution. In addition, there is an overbrightness in the disk continuum emission at this same azimuth. These asymmetries could be linked to

Table 3
Derived Column Densities, Abundance Ratios, and Rotational Temperatures for Molecules in the HD 100453 Disk

Molecule	$T_{\rm rot}$ (K)	$N_{\rm col}$ (cm^{-2})	$N_{\rm col}$ @ 228 K[a] (cm^{-2})	% of CH_3OH $N_{\rm col}$
CH_3OH	228^{+27}_{22}	$1.56^{+0.18}_{-0.14} \times 10^{16}$	…	…
$^{13}CH_3OH$	190^{+72}_{-67}	$7.50^{+0.51}_{-0.34} \times 10^{14}$	…	4.8 ± 0.6
CH_2DOH	…	…	$6.67^{+1.59}_{-1.58} \times 10^{14}$	4.3 ± 1.4
H_2CO	…	…	$6.13^{+0.55}_{-0.55} \times 10^{14}$	3.9 ± 0.5
$H_2^{13}CO$	…	…	$3.55^{+1.22}_{-1.22} \times 10^{13}$	0.2 ± 0.1
CH_3CN	50^{+17}_{-10}	$4.74^{+2.00}_{-1.10} \times 10^{13}$	…	0.3 ± 0.1
CH_3OCHO	…	…	$2.88^{+0.33}_{-0.25} \times 10^{14}$	1.9 ± 0.2
CH_3OCH_3	…	…	$<3.70 \times 10^{14}$	<2.4
HDO	…	…	$<6.25 \times 10^{14}$	<4.0

Note.

[a] Here 228 K is the rotational temperature derived from the CH_3OH.

shadowing from the inner disk, which is misaligned in both position and inclination angles (A. J. Bohn et al. 2022). The locations of the disk shadows due to this misalignment are qualitatively rotated ≈90° from the CO and CH_3OH hot spots, which supports this hypothesis if the molecule excesses are tracing the warmer gas outside the shadows. If the variation of the thermal structure of the disk is significant enough, this would lead to a cycle of desorption and adsorption of volatiles. Depending on the timescales on which the gas reacts to this change, it may be possible to see time-variable line emission from COMs, as the orbital timescale at 0.315 au, the peak emitting radius of the inner disk, is only 0.14 yr (A. J. Bohn et al. 2022).

On larger scales, the HD 100453 disk is also known to have two spiral arms that are induced by an external binary companion (e.g., K. Wagner et al. 2018; G. P. Rosotti et al. 2020). In gas emission, these have been traced by optically thick CO lines; therefore, its hard to determine whether this is a total gas density enhancement or a temperature enhancement. In these data, we do not see any clear signatures of spirals traced in molecular lines, but given the spatial resolution of these data, this is not surprising. Interestingly, the ^{12}CO $J = 3$–2 spectra also show the same apparent excess in emission close to the source velocity as the CH_3OH. Therefore, instead of a small-scale temperature asymmetry near the dust cavity edge, as discussed above, this spectral feature could be linked to the spiral arms. The CH_3OH and H_2CO line strengths do mean that future high angular resolution (≈0.″1) observations are feasible, and this would enable a more detailed analysis into how we can use these molecules as density and temperature probes in this disk.

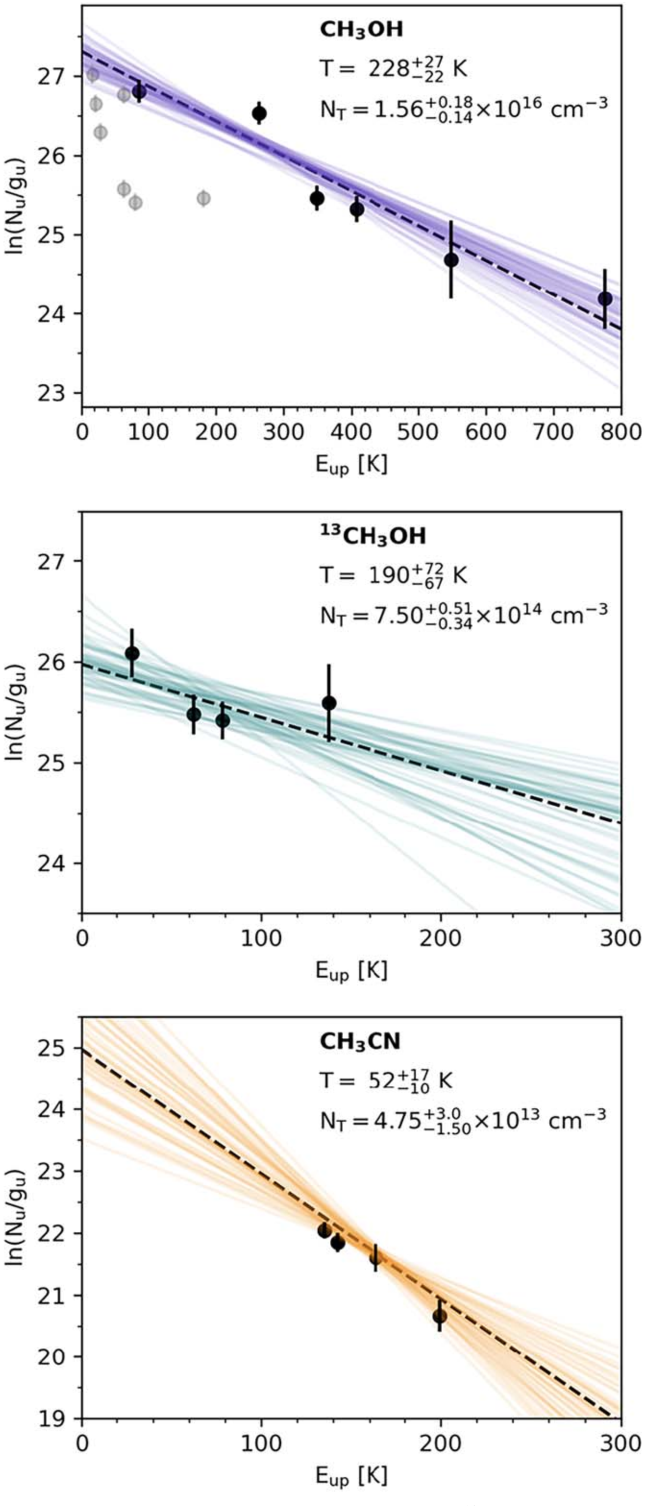

Figure 5. Disk-averaged rotation diagrams for CH_3OH, $^{13}CH_3OH$, and CH_3CN in the HD 100453 disk. The gray points in the CH_3OH plot show optically thicker transitions that are excluded from the linear fit. The dashed black lines show the best-fit model, and the colors show random draws from the corresponding posterior probability distributions.

4.2. Placing the HD 100453 COM Reservoir in Context

The combination of high upper energy level (>300 K) and low Einstein A-coefficient ($<10^{-4}$ s^{-1}) CH_3OH lines detected in this study allows us to make a robust measurement of the CH_3OH column density from optically thin lines. As a result, HD 100453 has a CH_3OH column density at least an order of magnitude higher when compared to other Class II disks, where reported values range from $\approx 10^{14}$ to 10^{15} cm^{-2} (A. S. Booth et al. 2023, 2024b; M. Temmink et al. 2025; L. Evans et al. 2025). The rotational temperature derived for CH_3OH in HD 100453 is warmer than the measurements for both the HD 100546 (≈150 K) and Oph-IRS 48 (≈125 K) disks (M. Temmink et al. 2025; L. Evans et al. 2025). The absolute values on the column densities do depend on assumptions regarding the emitting area, but the line coverage of the data here shows that these weaker

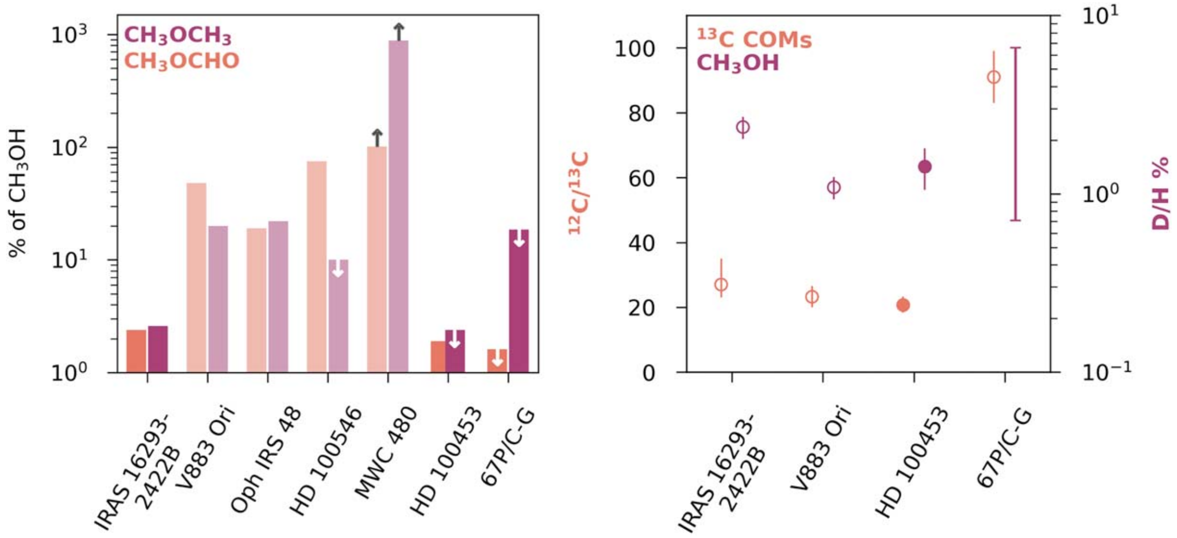

Figure 6. The abundances of various molecules in the HD 100453 disk compared to a selection of Class 0, I, and II objects, as well as the solar system comet 67P/C-G. Left: the abundances of CH_3OCH_3 and CH_3OCHO relative to CH_3OH, where arrows denote upper and lower limits. Here the Class II disks, aside from HD 100453, are translucent to indicate the uncertainty in the underlying CH_3OH column density. Right: the isotopic ratio of $^{12}C/^{13}C$ for COMs (all CH_3OH aside from IRAS 16293−2422 B, which is glycolaldehyde) and percentage D/H values for CH_3OH. The filled circles show the results from this work, and the open circles are values taken from the literature. For both panels, the data for the other sources are taken from J. K. Jørgensen et al. (2016, 2018), M. Rubin et al. (2019), K. Altwegg et al. (2020), M. N. Drozdovskaya et al. (2021), Y. Yamato et al. (2024a), A. S. Booth et al. (2024a, 2024b), and J.-H. Jeong et al. (2025).

lines are detectable in Class II disks, and therefore the column densities from these other studies may be underestimates. These sources should be revisited with more optically thin observations since abundances extracted from optically thick and optically thin lines have different dependencies on assumed emission areas.

In HD 100453, we find that CH_3OCHO is only present at the ≈2% level of CH_3OH, which is at least a factor of 10 lower than that measured toward other Class II disks and at least a factor of a few lower than that seen toward younger outbursting sources (A. S. Booth et al. 2024a, 2024b; J. K. Calahan et al. 2024; Y. Yamato et al. 2024b, 2024a; J.-H. Jeong et al. 2025). CH_3OCH_3 is not detected in the HD 100453 disk, but the upper limits relative to CH_3OCHO are not constraining. The difference in the HD 100453 COM abundances relative to CH_3OH is shown in Figure 6, where we compare the CH_3OCHO and CH_3OCH_3 column densities with those reported for three other Class II disks (HD 100546, Oph-IRS 48, and MWC 480), IRAS 16293−2422 B, V883 Ori, and comet 67P/C-G (where column destinies are taken from J. K. Jørgensen et al. 2016, 2018; M. Rubin et al. 2019; A. S. Booth et al. 2024a, 2024b; J.-H. Jeong et al. 2025). This percent level abundance is more consistent with the values seen in the warm gas phase toward younger systems (e.g., J. B. Bergner et al. 2017; M. L. van Gelder et al. 2020; S. Manigand et al. 2020). This result may support the intact inheritance of COMs in disks rather than the in situ processing of inherited CH_3OH into other COMs as proposed for the other Class II disks (e.g., A. S. Booth et al. 2024a, 2024b). It is not clear yet what the intrinsic variation in COM reservoirs across Class II disks is or whether the high abundances seen in other works may be due to an underappreciation of optical depth effects impacting the derived CH_3OH column densities.

After TW Hya, HD 100453 is the second Class II disk so far where both CH_3OH and CH_3CN have been detected. Looking at the relative abundance of CH_3CN seen toward protostars, our CH_3CN/CH_3OH abundance of ≈0.3% is within the ranges seen in this warmer environment (e.g., J. B. Bergner et al. 2017; P. Nazari et al. 2021) and approximately an order of magnitude lower than that of 67P/C-G (M. Rubin et al. 2019). When comparing HD 100453 to the transition disks HD 100546 and Oph-IRS 48, where CH_3CN has gone undetected, the upper limits relative to CH_3OH show that deeper data are needed to detect this potential reservoir of nitrogen-rich COMs in these other disks (A. S. Booth et al. 2024a, 2024b). Interestingly, the rotational temperature for CH_3CN in HD 100453 is significantly cooler than that for CH_3OH, bringing into question whether this is indeed an ice sublimation product, given that these two species have similar binding energies (M. Minissale et al. 2022). Instead, these molecules may be tracing different radial and/or vertical regions of the disk.

The presence of COMs in Class II disks has also been used as a tracer of the gas-phase C/O, where in particular the molecules CH_3OH and CH_3CN have been shown to trace environments of $C/O \approx 0.5$ and $C/O > 1$, respectively (A. S. Booth et al. 2023; J. K. Calahan et al. 2023). The lack of C_2H in the HD 100453 system (G. V. Smirnov-Pinchukov et al. 2022) indicates that the disk gas has a $C/O \leqslant 1$, i.e., there is no relative excess of gas-phase carbon as seen in other systems. The detection of CH_3CN therefore may be somewhat at odds with the scenario presented in J. K. Calahan et al. (2023). We interpret the cooler CH_3CN gas as originating from a different physical region of the disk than the CH_3OH. Therefore, we could be seeing a radial change in C/O where the drop in rotational temperature of the CH_3CN compared to the CH_3OH indicates that this species is tracing cooler gas beyond the water snowline, where $C/O \approx 0.8$–1.0.

4.3. *Exploring the ^{13}C Ratio in Disk Organics*

With the detection of $^{13}CH_3OH$, we now have a window into the $^{12}C/^{13}C$ ratio in the disk's large organic reservoir. In Class II disks the most complete information we have on the variation of $^{12}C/^{13}C$ across different molecular families is from observations of the TW Hya protoplanetary disk as collated by E. A. Bergin et al. (2024). In TW Hya there are two distinct isotopic reservoirs for carbon where the CO gas is enhanced in ^{13}C within 110 au, whereas within the same radii the C_2H, CN, and HCN molecules are consistent with the local ISM abundances or somewhat depleted in ^{13}C (K. Zhang et al. 2017; P. Hily-Blant et al. 2019; T. C. Yoshida et al. 2022b, 2024; E. A. Bergin et al. 2024). This fractionation of carbon is proposed to happen in the gas phase and, depending on the height in the disk, is driven by isotope-selective photodissociation or cosmic-ray ionization closer to the midplane, where the low-temperature carbon isotopic fractionation reaction(s) are active (D. Smith & N. G. Adams 1980; P. M. Woods & K. Willacy 2009; E. A. Bergin et al. 2024). There is also a C/O dependence where the gas-phase isotope exchange reactions are more efficient in regimes where $C/O > 1$ (W. D. Langer et al. 1984; T. C. Yoshida et al. 2022a; S. Lee et al. 2024). For the larger organics that are chemically derived from CO, such as H_2CO and CH_3OH, which can form efficiently on grain surfaces, the potential in situ carbon isotopic fractionation in disks has yet to be explored in detail from either an observational or a modeling perspective. $H_2^{13}CO$ has been detected in the Oph-IRS 48 and HD 100546 disks (A. S. Booth et al. 2024a, 2024b), and for HD 100546 in particular, the $H_2^{13}CO$ is detected in the outer disk ring, where the H_2CO is optically thin and cold, ≈30 K (L. Evans et al. 2025). From the HD 100546 data presented in A. S. Booth et al. (2024a) there is the indication of a ≈2× enhancement in ^{13}C in H_2CO relative to the ISM, but higher signal-to-noise ratio data are needed to confirm.

For the HD 100453 disk we can measure the $^{12}C/^{13}C$ ratio in CO, H_2CO, and CH_3OH. Unfortunately, the isotopic ratios in CO and H_2CO are difficult to constrain here owing to the high optical depth of $C^{18}O$ (e.g., L. M. Stapper et al. 2024) and the tentative nature of the $H_2^{13}CO$ detection. From the disk-integrated column densities we find a lower limit $^{12}C/^{13}C$ in H_2CO of >17. For CH_3OH we find a $^{12}C/^{13}C$ ratio of 21 ± 3, which is a ≈3× enhancement in ^{13}C relative to the local ISM value of 69 (T. L. Wilson 1999). As shown in Figure 6, this level of enhancement in ^{13}C has also been seen in the CH_3OH and other COMs from the outbursting Class I source V883 Ori (J.-H. Jeong et al. 2025; Y. Yamato et al. 2024b), possibly in the CH_3OH in the Class 0 HH 212 disk (C.-F. Lee et al. 2019), and in the glycolaldehyde detected in the Class O IRAS 16293 −2422 B (J. K. Jørgensen et al. 2016). Interestingly, in comparison, the ^{13}C in comet 67P/C-G is consistent with the solar value of 91, which is somewhat depleted relative to the local ISM (K. Altwegg et al. 2020). Such a clear signature of isotopic fractionation in the ices in molecular clouds and protostellar envelopes has so far eluded detection in CO and CO_2 ices (M. K. McClure et al. 2023; N. G. C. Brunken et al. 2024). This indicates that the enhancement of ^{13}C in CO and other CO-derived organics may take place within the disk environment rather than being inherited from earlier times and/or that there are different isotopic reservoirs in the simple molecules versus the (complex) organics. The enrichment of ^{13}C in organics may provide an answer to the overabundant ^{13}CO traced in giant exoplanet atmospheres (Y. Zhang et al. 2021).

4.4. Are We Tracing Inherited Ices?

The level of inheritance for disk organics can be evaluated based on the overall organic composition and the isotopic ratios among key organics. In addition to CH_3OH and $^{13}CH_3OH$, we also identify CH_2DOH for the first time in a Class II disk. From these data we find a D/H value in CH_3OH of 1%–2%, which, as shown in Figure 6, is consistent with the deuterium enhancement in CH_3OH observed toward prestellar cores and protostars (e.g., S. Manigand et al. 2020; H. E. Ambrose et al. 2021; M. L. van Gelder et al. 2022; Y. Lin et al. 2023), as well as the young disk V883 Ori, the HH 212 disk, and solar system comets (C.-F. Lee et al. 2019; M. N. Drozdovskaya et al. 2021; J.-H. Jeong et al. 2025). Given the low formation efficiency of CH_3OH in warm Herbig disks (A. S. Booth et al. 2021), the in situ deuteration of CH_3OH is unlikely but should be tested with future chemical modeling efforts. That being said, this result adds to growing evidence that Class II disks at least partially inherit icy material from the earlier stages of star formation.

Given the rotational temperature of the CH_3OH, we are likely tracing gas within the H_2O snowline, and thus H_2O should be observable in the gas phase too. We report an upper limit on the heavy water isotopologue HDO of <4% that of CH_3OH. Comparing this to the detections in protostars, outbursting sources, and comets (as collated in J. K. Calahan et al. 2024), these data are not sensitive enough to trace this avenue of ice inheritance. Future data to target more favorable H_2O (isotopologue) lines as predicted by S. Notsu et al. (2019) and seen in other systems (J. J. Tobin et al. 2023; S. Facchini et al. 2024) are necessary to make this much-needed connection.

5. Conclusion

In this work, we have presented the analysis of line-rich ALMA observations toward the HD 100453 protoplanetary disk. Our main conclusions are as follows:

1. The abundant CH_3OH detected is consistent with a ring of thermally sublimating ices located at the inner edge of the dust ring at ≈16 au. This CH_3OH emission is likely originating from within the H_2O snowline and is tracing gas with a $C/O < 1$. Additionally, there is evidence for an overbrightness along the disk minor axis that may be linked to shadowing due to a known misaligned inner disk on sub-au scales.
2. For the first time in a Class II disk we detect $^{13}CH_3OH$ and infer from this an enhanced ^{13}C abundance relative to the local ISM. This ≈3× increase is consistent with the high ^{13}C content of COMs in the V883 Ori disk, the CO gas in the TW Hya disk, and the CO measurements of gas giant exoplanet atmospheres.
3. With the tentative detection of CH_2DOH, we can also make the first measurement of the D/H ratio in Class II disk organics. We find a D/H value of ≈1%–2%, which is consistent with what is seen for CH_3OH toward low-mass prestellar cores, protostars, young Class I disks, and solar system comets, adding further evidence to support the presence of inherited interstellar ices in disks.
4. The detection of CH_3CN makes HD 100453 only the second Class II disk where both CH_3CN and CH_3OH have been detected. Interestingly, the CH_3CN is emitting from a much cooler gas reservoir than the CH_3OH, consistent with what has been measured for other Class II disks, where the $C/O > 1$ rather than the oxygen-rich gas present in this system.

5. The larger COM CH_3OCHO is detected, but the relative abundance with respect to CH_3OH is an order of magnitude lower than that reported for other Class II disks. In comparison, this lower value is more consistent with younger protostellar systems and may be due to the detection of weaker and higher energy level transitions of CH_3OH, which lead to an overall higher reported CH_3OH column density.
6. Finally, we report a nondetection of the heavy water isotopologue HDO and find that the derived upper limit is not constraining when compared to the abundances measured in other interstellar environments. Future data targeting more favorable transitions are needed to elucidate the nature of the cool water reservoir in disks as probed by ALMA.

HD 100453 is now the fifth disk around a Herbig Ae (or young F-type) star where thermally sublimating COMs have been detected (A. S. Booth et al. 2021; N. van der Marel et al. 2021; A. S. Booth et al. 2023; Y. Yamato et al. 2024a). These disks clearly give us access to a new complex organic and isotopic reservoir that has so far been inaccessible in cooler and lower-mass T Tauri disks. Therefore, ALMA observations of these systems are crucial in unraveling the history and inheritance of organics through the star, disk, and planet formation process.

Acknowledgments

This Letter makes use of the following ALMA data: 2017.1.01424.S, 2023.1.00252.S. ALMA is a partnership of ESO (representing its member states), NSF (USA) and NINS (Japan), together with NRC (Canada), MOST and ASIAA (Taiwan), and KASI (Republic of Korea), in cooperation with the Republic of Chile. The Joint ALMA Observatory is operated by ESO, AUI/NRAO and NAOJ. This work has used the following additional software packages that have not been referred to in the main text: Astropy, IPython, Jupyter, Matplotlib, and NumPy (Astropy Collaboration et al. 2022; F. Pérez & B. E. Granger 2007; T. Kluyver et al. 2016; J. D. Hunter 2007; C. R. Harris et al. 2020). A.S.B. is supported by a Clay Postdoctoral Fellowship from the Smithsonian Astrophysical Observatory. M.L. is funded by the European Union (ERC, UNVEIL, 101076613). Views and opinions expressed are, however, those of the author(s) only and do not necessarily reflect those of the European Union or the European Research Council. Neither the European Union nor the granting authority can be held responsible for them. Support for C.J.L. was provided by NASA through the NASA Hubble Fellowship grant No. HST-HF2-51535.001-A awarded by the Space Telescope Science Institute, which is operated by the Association of Universities for Research in Astronomy, Inc., for NASA, under contract NAS5-26555. S.N. is grateful for support from Grants-in-Aid for JSPS (Japan Society for the Promotion of Science) Fellows grant No. JP23KJ0329, MEXT/JSPS Grants-in-Aid for Scientific Research (KAKENHI) grant Nos. JP23K13155 and JP24K00674, and Start-up Research Grant as one of The University of Tokyo Excellent Young Researcher 2024. C.W. acknowledges financial support from the Science and Technology Facilities Council and UK Research and Innovation (grant Nos. ST/X001016/1 and MR/T040726/1).

ORCID iDs

Alice S. Booth https://orcid.org/0000-0003-2014-2121
Lisa Wölfer https://orcid.org/0000-0002-7212-2416
Milou Temmink https://orcid.org/0000-0002-7935-7445
Jenny Calahan https://orcid.org/0000-0002-0150-0125
Lucy Evans https://orcid.org/0009-0006-1929-3896
Charles J. Law https://orcid.org/0000-0003-1413-1776
Margot Leemker https://orcid.org/0000-0003-3674-7512
Shota Notsu https://orcid.org/0000-0003-2493-912X
Karin Öberg https://orcid.org/0000-0001-8798-1347
Catherine Walsh https://orcid.org/0000-0001-6078-786X

References

Allamandola, L. J., Sandford, S. A., & Valero, G. J. 1988, Icar, 76, 225
Altwegg, K., Balsiger, H., Combi, M., et al. 2020, MNRAS, 498, 5855
Ambrose, H. E., Shirley, Y. L., & Scibelli, S. 2021, MNRAS, 501, 347
Astropy Collaboration, Price-Whelan, A. M., Lim, P. L., et al. 2022, ApJ, 935, 167
Benisty, M., Stolker, T., Pohl, A., et al. 2017, A&A, 597, A42
Bergin, E. A., Bosman, A., Teague, R., et al. 2024, ApJ, 965, 147
Bergner, J. B., Guzmán, V. G., Öberg, K. I., Loomis, R. A., & Pegues, J. 2018, ApJ, 857, 69
Bergner, J. B., Öberg, K. I., Garrod, R. T., & Graninger, D. M. 2017, ApJ, 841, 120
Bertin, M., Romanzin, C., Doronin, M., et al. 2016, ApJL, 817, L12
Bohn, A. J., Benisty, M., Perraut, K., et al. 2022, A&A, 658, A183
Booth, A. S., Law, C. J., Temmink, M., Leemker, M., & Macías, E. 2023, A&A, 678, A146
Booth, A. S., Leemker, M., van Dishoeck, E. F., et al. 2024a, AJ, 167, 164
Booth, A. S., Temmink, M., van Dishoeck, E. F., et al. 2024b, AJ, 167, 165
Booth, A. S., Walsh, C., Terwisscha van Scheltinga, J., et al. 2021, NatAs, 5, 684
Brunken, N. G. C., Booth, A. S., Leemker, M., et al. 2022, A&A, 659, A29
Brunken, N. G. C., van Dishoeck, E. F., Slavicinska, K., et al. 2024, A&A, 692, A163
Calahan, J. K., Bergin, E. A., Bosman, A. D., et al. 2023, NatAs, 7, 49
Calahan, J. K., Bergin, E. A., van't Hoff, M., et al. 2024, ApJ, 975, 170
Carney, M. T., Hogerheijde, M. R., Guzmán, V. V., et al. 2019, A&A, 623, A124
Collins, K. A., Grady, C. A., Hamaguchi, K., et al. 2009, ApJ, 697, 557
Drozdovskaya, M. N., Schroeder I, I. R. H. G., Rubin, M., et al. 2021, MNRAS, 500, 4901
Drozdovskaya, M. N., Walsh, C., Visser, R., Harsono, D., & van Dishoeck, E. F. 2014, MNRAS, 445, 913
Evans, L., Booth, A. S., Walsh, C., et al. 2025, ApJL, 982, 62
Facchini, S., Testi, L., Humphreys, E., et al. 2024, NatAs, 8, 587
Favre, C., Fedele, D., Semenov, D., et al. 2018, ApJL, 862, L2
Foreman-Mackey, D., Hogg, D. W., Lang, D., & Goodman, J. 2013, PASP, 125, 306
Gerakines, P. A., Schutte, W. A., & Ehrenfreund, P. 1996, A&A, 312, 289
Guzmán-Díaz, J., Mendigutía, I., Montesinos, B., et al. 2021, A&A, 650, A182
Harris, C. R., Millman, K. J., van der Walt, S. J., et al. 2020, Natur, 585, 357
Herbst, E., & van Dishoeck, E. F. 2009, ARA&A, 47, 427
Hily-Blant, P., Magalhaes de Souza, V., Kastner, J., & Forveille, T. 2019, A&A, 632, L12
Hunter, J. D. 2007, CSE, 9, 90
Ilee, J. D., Walsh, C., Booth, A. S., et al. 2021, ApJS, 257, 9
Jeong, J.-H., Lee, J.-E., Lee, S., et al. 2025, ApJS, 276, 49
Jørgensen, J. K., Belloche, A., & Garrod, R. T. 2020, ARA&A, 58, 727
Jørgensen, J. K., Müller, H. S. P., Calcutt, H., et al. 2018, A&A, 620, A170
Jørgensen, J. K., van der Wiel, M. H. D., Coutens, A., et al. 2016, A&A, 595, A117
Kluyver, T., Ragan-Kelley, B., Pérez, F., et al. 2016, in Positioning and Power in Academic Publishing: Players, Agents and Agendas, ed. F. Loizides & B. Schmidt (Amsterdam: IOS Press), 87
Langer, W. D., Graedel, T. E., Frerking, M. A., & Armentrout, P. B. 1984, ApJ, 277, 581
Lee, C.-F., Codella, C., Li, Z.-Y., & Liu, S.-Y. 2019, ApJ, 876, 63
Lee, S., Nomura, H., & Furuya, K. 2024, ApJ, 969, 41
Lin, Y., Spezzano, S., & Caselli, P. 2023, A&A, 669, L6
Loomis, R. A., Cleeves, L. I., Öberg, K. I., et al. 2018a, ApJ, 859, 131
Loomis, R. A., Öberg, K. I., Andrews, S. M., et al. 2018b, AJ, 155, 182
Manigand, S., Jørgensen, J. K., Calcutt, H., et al. 2020, A&A, 635, A48
McClure, M. K., Rocha, W. R. M., Pontoppidan, K. M., et al. 2023, NatAs, 7, 431
McMullin, J. P., Waters, B., Schiebel, D., Young, W., & Golap, K. 2007, in ASP Conf. Ser. 376, Astronomical Data Analysis Software and Systems XVI, ed. R. A. Shaw, F. Hill, & D. J. Bell (San Francisco, CA: ASP), 127

Minissale, M., Aikawa, Y., Bergin, E., et al. 2022, ESC, 6, 597
Müller, H. S. P., Schlöder, F., Stutzki, J., & Winnewisser, G. 2005, JMoSt, 742, 215
Müller, H. S. P., Thorwirth, S., Roth, D. A., & Winnewisser, G. 2001, A&A, 370, L49
Nazari, P., van Gelder, M. L., van Dishoeck, E. F., et al. 2021, A&A, 650, A150
Notsu, S., Akiyama, E., Booth, A., et al. 2019, ApJ, 875, 96
Öberg, K. I., Garrod, R. T., van Dishoeck, E. F., & Linnartz, H. 2009, A&A, 504, 891
Öberg, K. I., Guzmán, V. V., Furuya, K., et al. 2015, Natur, 520, 198
Pegues, J., Öberg, K. I., Bergner, J. B., et al. 2020, ApJ, 890, 142
Pérez, F., & Granger, B. E. 2007, CSE, 9, 21
Pickett, H. M., Poynter, R. L., Cohen, E. A., et al. 1998, JQSRT, 60, 883
Rosotti, G. P., Benisty, M., Juhász, A., et al. 2020, MNRAS, 491, 1335
Rubin, M., Altwegg, K., Balsiger, H., et al. 2019, MNRAS, 489, 594
Scibelli, S., Shirley, Y., Vasyunin, A., & Launhardt, R. 2021, MNRAS, 504, 5754
Smirnov-Pinchukov, G. V., Moór, A., Semenov, D. A., et al. 2022, MNRAS, 510, 1148
Smith, D., & Adams, N. G. 1980, ApJ, 242, 424
Stapper, L. M., Hogerheijde, M. R., van Dishoeck, E. F., et al. 2024, A&A, 682, A149
Taquet, V., López-Sepulcre, A., Ceccarelli, C., et al. 2015, ApJ, 804, 81
Temmink, M., Booth, A. S., Leemker, M., et al. 2025, A&A, 693, A101
Temmink, M., Booth, A. S., van der Marel, N., & van Dishoeck, E. F. 2023, A&A, 675, A131
Tobin, J. J., van't Hoff, M. L. R., Leemker, M., et al. 2023, Natur, 615, 227
van der Marel, N., Booth, A. S., Leemker, M., van Dishoeck, E. F., & Ohashi, S. 2021, A&A, 651, L5
van der Plas, G., Ménard, F., Gonzalez, J. F., et al. 2019, A&A, 624, A33
van Gelder, M. L., Jaspers, J., Nazari, P., et al. 2022, A&A, 667, A136
van Gelder, M. L., Tabone, B., Tychoniec, Ł., et al. 2020, A&A, 639, A87
Wagner, K., Apai, D., Kasper, M., & Robberto, M. 2015, ApJL, 813, L2
Wagner, K., Dong, R., Sheehan, P., et al. 2018, ApJ, 854, 130
Walsh, C., Herbst, E., Nomura, H., Millar, T. J., & Weaver, S. W. 2014, FaDi, 168, 389
Walsh, C., Loomis, R. A., Öberg, K. I., et al. 2016, ApJL, 823, L10
Walsh, C., Vissapragada, S., & McGee, H. 2018, in IAU Symp. 332, ed. M. Cunningham, T. Millar, & Y. Aikawa (Cambridge: Cambridge Univ. Press), 395
Wilson, T. L. 1999, RPPh, 62, 143
Wölfer, L., Facchini, S., van der Marel, N., et al. 2023, A&A, 670, A154
Woods, P. M., & Willacy, K. 2009, ApJ, 693, 1360
Yamato, Y., Aikawa, Y., Guzmán, V. V., et al. 2024a, ApJ, 974, 83
Yamato, Y., Notsu, S., Aikawa, Y., et al. 2024b, AJ, 167, 66
Yoshida, T. C., Nomura, H., Furuya, K., Tsukagoshi, T., & Lee, S. 2022a, ApJ, 932, 126
Yoshida, T. C., Nomura, H., Furuya, K., et al. 2024, ApJ, 966, 63
Yoshida, T. C., Nomura, H., Tsukagoshi, T., Furuya, K., & Ueda, T. 2022b, ApJL, 937, L14
Zhang, K., Bergin, E. A., Blake, G. A., Cleeves, L. I., & Schwarz, K. R. 2017, NatAs, 1, 0130
Zhang, Y., Snellen, I. A. G., Bohn, A. J., et al. 2021, Natur, 595, 370